

Leveraging the Doppler Effect for Channel Charting

Florian Euchner¹, Phillip Stephan¹, Stephan ten Brink¹

Institute of Telecommunications, Pfaffenwaldring 47, University of Stuttgart, 70569 Stuttgart, Germany
{euchner,stephan,tenbrink}@inue.uni-stuttgart.de

Abstract—Channel Charting is a dimensionality reduction technique that reconstructs a map of the radio environment from similarity relationships found in channel state information. Distances in the channel chart are often computed based on some dissimilarity metric, which can be derived from angular-domain information, channel impulse responses, measured phase differences or simply timestamps. Using such information implicitly makes strong assumptions about the level of phase and time synchronization between base station antennas or assumes approximately constant transmitter velocity. Many practical systems, however, may not provide phase and time synchronization and single-antenna base stations may not even have angular-domain information. We propose a Doppler effect-based loss function for Channel Charting that only requires frequency synchronization between spatially distributed base station antennas, which is a much weaker assumption. We use a dataset measured in an indoor environment to demonstrate that the proposed method is practically feasible with just four base station antennas, that it produces a channel chart that is suitable for localization in the global coordinate frame and that it outperforms other state-of-the-art methods under the given limitations.

Index Terms—Channel Charting, Doppler effect, localization

I. INTRODUCTION

Channel Charting [1] is a self-supervised dimensionality reduction method that learns the forward charting function (FCF), a mapping from high-dimensional channel state information (CSI) to a low-dimensional representation, the so-called channel chart, which can be interpreted as a map of the radio environment. It relies on similarity relationships in measured CSI, thus exploiting the multipath characteristics of the propagation environment. Initially, Channel Charting was proposed primarily as a technique for *relative* localization, i.e., only achieving local spatial consistency, but additional work [2], [3] suggested that even the *global* geometry could be preserved and that Channel Charting in absolute global coordinates is possible as long as the location of base station (BS) antennas is known [4]–[6]. Previous work on Channel Charting in global coordinates assumed a large number of time- and phase-synchronized antennas, with a total of 80 BS antennas in [4], and 32 BS antennas in [5] and [6]. Here, we implement Channel Charting in global coordinates with only 4 BS antennas and without time or phase synchronization, by leveraging Doppler effect-induced phase changes¹.

The classical problem of source localization and velocity estimation for an active transmitter based on Doppler shift mea-

surements from a spatially distributed sensor network is well-known and has been thoroughly investigated, e.g., in [7], [8]. Their work uses Doppler shift measurements to not only estimate the transmitter’s velocity, but also its location and carrier frequency offset (CFO). However, classical solutions to this problem, which optimize a cost function parametrized on individual frequency shift measurements, have several shortcomings: For example, [7] assumes a nonmaneuvering transmitter, i.e., a constant transmitter velocity over a certain timespan. The approach in [8], on the other hand, needs Doppler shift measurements at five or more locations to solve for the unknown variables (CFO, position and velocity in two dimensions), even in the noiseless case. In contrast to that, our proposed Channel Charting-based approach can locate users with fewer BS antennas. It learns the FCF, implemented as a neural network, from a large number of observations and then uses that FCF for localization. Whereas the classical approaches only work *while* the transmitter is moving, our Channel Charting-based technique, once trained on moving transmitters, will continue to function for static transmitters.

II. DATASET AND SYSTEM MODEL

In our system model, we have a single transmitter, called user equipment (UE), and several frequency-synchronized and spatially distributed receiver antennas (single-antenna BSs). In practice, frequency synchronization among BS antennas can be achieved by distributing a reference clock signal, by exchanging over-the-air synchronization messages, or by relying on time sources like GPS disciplined oscillators (GPSDOs). A central challenge in Doppler effect-based radio localization is the unknown and variable transmit frequency. While the carrier frequency should ideally be well-defined, it is usually derived from a crystal oscillator, which can exhibit large offsets and drifts. A typical crystal oscillator can have a frequency offset of ± 20 ppm, corresponding to a CFO-induced frequency shift of $f_{\text{CFO}} = \pm 20$ kHz even at a low carrier frequency of 1 GHz. At that frequency, moving at a velocity of $1 \frac{\text{m}}{\text{s}}$ leads to a Doppler shift of just around ± 3.3 Hz! A Doppler effect-based localization system must hence be robust against CFO.

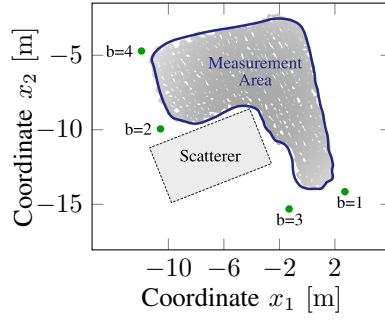
The considered indoor factory environment dataset, known as *dichasus-cf0x*, was already used in previous work on Channel Charting [3], [6], [9], [10]. The dataset was generated by *Distributed Channel Sounder by University of Stuttgart (DICHASUS)*, our distributed massive multiple-input multiple-output (mMIMO) channel sounder, whose architecture is described in [11]. In brief, DICHASUS measures the channel between the UE and all BS antennas. DICHASUS provides large

This work is supported by the German Federal Ministry of Education and Research (BMBF) within the projects Open6GHub (grant no. 16KISK019) and KOMSENS-6G (grant no. 16KISK113).

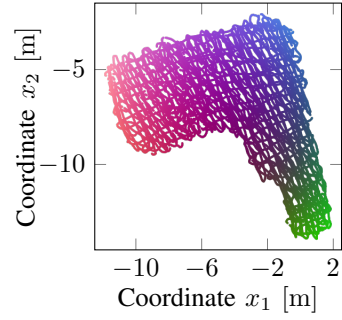
¹Partial source code and the dataset for this paper are publicly available at <https://github.com/Jeija/Doppler-Effect-ChannelCharting/>



(a)



(b)



(c)

Fig. 1. Information about the environment the dataset was measured in: The figure shows (a) a photograph of the environment, (b) a top view map and (c) a scatter plot of colored “ground truth” positions (only used for evaluation, not training) of datapoints in $\mathcal{S}_{\text{train}}$.

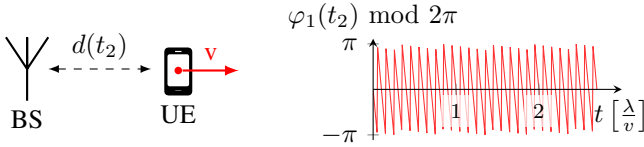


Fig. 2. Single BS antenna, unsynchronized UE moving at velocity v away from BS: Received uplink phase is affected by both CFO and Doppler shift.

datasets containing frequency-domain channel coefficients, alongside timestamps and accurate position information. For *dichasus-cf0x*, $B = 4$ receiver antenna arrays with 2×4 antennas each are set up in a factory hall, and $N_{\text{sub}} = 1024$ orthogonal frequency division multiplex (OFDM) channel coefficients are measured at a carrier frequency of 1.272 GHz and with a total bandwidth of 50 MHz. The $B = 4$ antennas are known to be located at $\mathbf{z}^{(b)} \in \mathbb{R}^3$. Here, we only use CSI from one antenna per array, and we arbitrarily pick the third antenna in the first row of each array. Hence, the resulting CSI can be represented as a matrix $\mathbf{H}^{(l)} \in \mathbb{C}^{B \times N_{\text{sub}}}$ containing complex-valued channel coefficients of all $B = 4$ BS antennas and all N_{sub} subcarriers for time instance l . $\mathcal{F}^{-1}\{\mathbf{H}^{(l)}\}$ denotes the inverse discrete Fourier transform of the CSI matrix along the frequency axis, i.e., the antenna-specific channel impulse responses (CIRs).

The transmitter is a dipole antenna which is mounted on top of a robot, traveling at a median speed of approximately $0.25 \frac{\text{m}}{\text{s}}$ along a set of trajectories inside an L-shaped area, with an overall bounding box size of approximately $14 \text{ m} \times 14 \text{ m}$. A prism is attached to the tip of the transmit antenna and tracked with millimeter-level precision by a tachymeter, providing “ground truth” positions $\mathbf{x}^{(l)}$. In all localization tasks, we assume that the height of the transmitter, $x_3^{(l)}$, is known and constant, which simplifies the problem to two-dimensional localization. In addition to CSI and reference positions, timestamps $t^{(l)}$ as well as instantaneous, BS antenna-specific frequency offset measurements $\mathbf{f}^{(l)} \in \mathbb{R}^B$ are collected. Thus, the complete dataset can be represented as the following set containing a total of L datapoints:

$$\text{Dataset} : \mathcal{S} = \left\{ \left(\mathbf{H}^{(l)}, \mathbf{x}^{(l)}, t^{(l)}, \mathbf{f}^{(l)} \right) \right\}_{l=1, \dots, L}$$

For evaluation purposes, the dataset \mathcal{S} is split into a training set $\mathcal{S}_{\text{train}}$ and a test set $\mathcal{S}_{\text{test}}$ containing $|\mathcal{S}_{\text{train}}| = |\mathcal{S}_{\text{test}}| =$

20851 datapoints each. A photo and a top view map of the environment are shown in Fig. 1. The true datapoint positions $\mathbf{x}^{(l)}$ are shown in Fig. 1c. The points have been colored and the datapoints will retain their color even as the FCF maps them to a position in the channel chart. This allows for a visual evaluation of the generated chart: If the global topology is preserved, a similar color gradient should appear in the chart.

Thanks to an elaborate over-the-air synchronization technique [11], [12], DICHASUS achieves frequency, time and phase coherence across all spatially distributed antennas. However, to support the claim that the Doppler effect-based localization technique works even without phase and time synchronization, we remove the fine time synchronization and randomize the initial phase for the feature vectors provided to the neural network. Under these circumstances, time of arrival (ToA)-based positioning would not work. Furthermore, with only one antenna at each BS site, angular-domain information is not available either, rendering angle of arrival (AoA)-based positioning infeasible. Common Channel Charting techniques and dissimilarity metrics [1]–[3] equally fail due to making assumptions about synchronization. We want to point out that carrier and sampling frequency synchronization implies phase and time synchronization down to constant offsets over short time intervals. However, we acknowledge that the frequency synchronization may be imperfect, i.e., phases and sampling times may drift over longer time intervals. Furthermore, phase locked loop (PLL)-based frequency synthesizers are another well-known source of output phase ambiguity [13], causing loss of time and phase synchronization when the PLL re-locks.

III. DOPPLER EFFECT-BASED LOSS FUNCTION

In the following, we derive a loss function for training the neural network (NN) that implements the FCF. Since our loss function operates on pairs of positions, it is particularly suited for training the FCF embedded into a Siamese NN configuration.

A. Introduction: Doppler Effect and Cumulative Phases

The causes for aforementioned observed frequency offsets $\mathbf{f} \in \mathbb{R}^B$, stored the dataset, are twofold: The CFO between UE and BS antennas f_{CFO} , and the antenna-specific Doppler shift $f_{\text{Dop},b}$, $b \in \{1, \dots, B\}$ where usually $|f_{\text{CFO}}| \gg |f_{\text{Dop},b}|$.

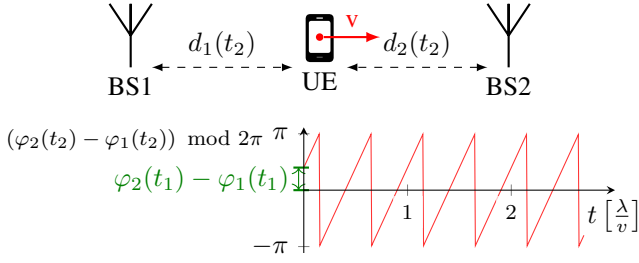


Fig. 3. Two BS antennas, UE moving at velocity v between BS antennas. The change in differential uplink phases, caused by the Doppler effect, is now unaffected by CFO. λ denotes the wavelength. The figure assumes $t_1 = 0$.

Assuming a free space channel model, the frequency offset caused by the movement of the UE in space leads to a change in the received phase at the BS b . In a continuous-time model, the received phase at time t_2 can be described as

$$\begin{aligned} \varphi_b(t_2) &= \int_{t_1}^{t_2} 2\pi f_b(t) dt = \int_{t_1}^{t_2} 2\pi (f_{\text{CFO}}(t) + f_{\text{Dop},b}(t)) dt \\ &= \varphi_b(t_1) + \varphi_{\text{CFO}}(t_2) + \varphi_{\text{Dop},b}(t_2), \end{aligned} \quad (1)$$

where $\varphi_b(t_1)$ is the initial phase for BS b at time t_1 , $\varphi_{\text{CFO}}(t_2)$ denotes the CFO-induced phase change and $\varphi_{\text{Dop},b}(t_2)$ denotes the BS antenna-specific phase change caused by the Doppler effect. We always assume $t_2 \geq t_1$ without loss of generality. Due to the large and unknown CFO, $\varphi_b(t_2)$ by itself is not useful for localization or velocity estimation, as illustrated in Fig. 2: The phase drift due to CFO far outpaces the phase change caused by movement. However, the *difference* in phase changes $\varphi_b(t_2)$ between two BSs b_1 and b_2 is unaffected by CFO, since both BS antennas, being frequency-synchronized, observe the same CFO:

$$\begin{aligned} \varphi_{b_2}(t_2) - \varphi_{b_1}(t_2) \\ = \varphi_{b_2}(t_1) - \varphi_{b_1}(t_1) + \varphi_{\text{Dop},b_2}(t_2) - \varphi_{\text{Dop},b_1}(t_2). \end{aligned} \quad (2)$$

This is visualized in the one-dimensional model in Fig. 3, where the rate of change in the received phase differences (i.e., the angular frequency) could be used to estimate the velocity v of the UE. We realize that $\frac{\lambda}{2\pi}(\varphi_{\text{Dop},b}(t_2) - \varphi_{\text{Dop},b}(t_1))$ is the change in distance between UE and BS antenna b when a Doppler shift-induced phase change of $\varphi_{\text{Dop},b}(t_2) - \varphi_{\text{Dop},b}(t_1)$ is measured. By solving Eq. (2) for $\varphi_{\text{Dop},b_2}(t_2) - \varphi_{\text{Dop},b_1}(t_2)$ and assuming unwrapped phases, we can obtain an expression relating the phase change to the displacement of the UE in the time interval $[t_1, t_2]$:

$$\begin{aligned} &\varphi_{\text{Dop},b_2}(t_2) - \varphi_{\text{Dop},b_1}(t_2) \\ &= (\varphi_{b_2}(t_2) - \varphi_{b_1}(t_2)) - (\varphi_{b_2}(t_1) - \varphi_{b_1}(t_1)) \\ &= \frac{2\pi}{\lambda} [(d_{b_2}(t_2) - d_{b_1}(t_2)) - (d_{b_2}(t_1) - d_{b_1}(t_1))], \end{aligned} \quad (3)$$

where $d_b(t) = \|\hat{\mathbf{x}}(t) - \mathbf{z}^{(b)}\|_2$ denotes the spatial distance between BS b and supposed UE location $\hat{\mathbf{x}}(t)$ at time t .

B. In Discrete Time, Comparing Phases

Eq. (1) describes how $\varphi_b(t)$ is computed by integrating the observed frequency offsets over time. In practice, the fre-

quency offset measurements in our dataset are only available at discrete points in time, so we replace the integration with the corresponding summation taking into account differences in timestamps, and obtain the discrete-time phase measurements $\varphi_b^{(l)}$ at times $t^{(l)}$. In addition to the instantaneous frequency offset estimates $\mathbf{f}^{(l)}$ in the dataset, we update the integrated phases $\varphi_b^{(l)}$ based on the phase measurements in the CSI matrix $\mathbf{H}^{(l)}$, by comparing phases predicted based on $\mathbf{f}^{(l)}$ to phases actually measured in $\mathbf{H}^{(l)}$. This, of course, requires sufficiently frequent sampling, which is realistic for practical systems that may also transmit very frequently or continuously.

C. Log-Likelihood Function

We derive a log-likelihood function for pairs of datapoints (l_1, l_2) by generalizing a discrete-time version of Eq. (3) to more than two BS antennas. To this end, we assume that we have unwrapped phase measurements $\varphi_b^{(l)}$ and we assume an i.i.d. normally distributed error in the phase difference measurements $n_{b_1, b_2}^{(l_1, l_2)} \sim \mathcal{N}\left(0, \left(\sigma_{b_1, b_2}^{(l_1, l_2)}\right)^2\right)$, i.e.,

$$\begin{aligned} &(\varphi_{b_2}^{(l_2)} - \varphi_{b_1}^{(l_2)}) - (\varphi_{b_2}^{(l_1)} - \varphi_{b_1}^{(l_1)}) + n_{b_1, b_2}^{(l_1, l_2)} \\ &= \frac{2\pi}{\lambda} \left[(d_{b_2}^{(l_2)} - d_{b_1}^{(l_2)}) - (d_{b_2}^{(l_1)} - d_{b_1}^{(l_1)}) \right], \end{aligned}$$

where $d_b^{(l)} = \|\hat{\mathbf{x}}^{(l)} - \mathbf{z}^{(b)}\|_2$. We remark that the assumption of an i.i.d. error distribution is flawed, and may be revised in future versions. We let $f_{b_1, b_2}^{(l_1, l_2)}(\hat{\mathbf{x}}^{(l_1)}, \hat{\mathbf{x}}^{(l_2)})$ denote the corresponding likelihood function, based on the Gaussian probability density function of $n_{b_1, b_2}^{(l_1, l_2)}$. For any pair of datapoints (l_1, l_2) , based on the assumption of i.i.d. errors $n_{b_1, b_2}^{(l_1, l_2)}$, we find the overall likelihood for the pair of positions $(\mathbf{x}^{(l_1)}, \mathbf{x}^{(l_2)})$ taking into account all pairs of BS antennas to be

$$f^{(l_1, l_2)} = \prod_{b_1=1}^B \prod_{b_2=1}^B f_{b_1, b_2}^{(l_1, l_2)}.$$

Finally, we find the log-likelihood function (neglecting constant terms) $\mathcal{L}^{(l_1, l_2)} = \log f^{(l_1, l_2)}(\hat{\mathbf{x}}^{(l_1)}, \hat{\mathbf{x}}^{(l_2)}) - \text{const.}$ as

$$\mathcal{L}^{(l_1, l_2)} = \sum_{b_1=1}^B \sum_{b_2=1}^B \left(\frac{\Delta\varphi_{b_1, b_2}^{(l_1, l_2)} - \frac{2\pi}{\lambda} \Delta d_{b_1, b_2}^{(l_1, l_2)}}{\sigma_{b_1, b_2}^{(l_1, l_2)}} \right)^2, \quad (4)$$

where we use the abbreviations

$$\begin{aligned} \Delta\varphi_{b_1, b_2}^{(l_1, l_2)} &= (\varphi_{b_2}^{(l_2)} - \varphi_{b_1}^{(l_2)}) - (\varphi_{b_2}^{(l_1)} - \varphi_{b_1}^{(l_1)}) \quad \text{and} \\ \Delta d_{b_1, b_2}^{(l_1, l_2)} &= (d_{b_2}^{(l_2)} - d_{b_1}^{(l_2)}) - (d_{b_2}^{(l_1)} - d_{b_1}^{(l_1)}). \end{aligned} \quad (5)$$

Clearly, the log-likelihood function in Eq. (4) is suited for Siamese neural network-based Channel Charting, where a loss is computed based on pairs of position estimates $\hat{\mathbf{x}}^{(l_1)}$ and $\hat{\mathbf{x}}^{(l_2)}$. We remark that the phases $\varphi_b^{(l)}$, $b \in \{1, \dots, B\}$, which were integrated and unwrapped along the UE's trajectory, may be interpreted as a *path signature*. In that sense, our approach shares some similarities with the concept of using path signatures for Channel Charting outlined in [14].

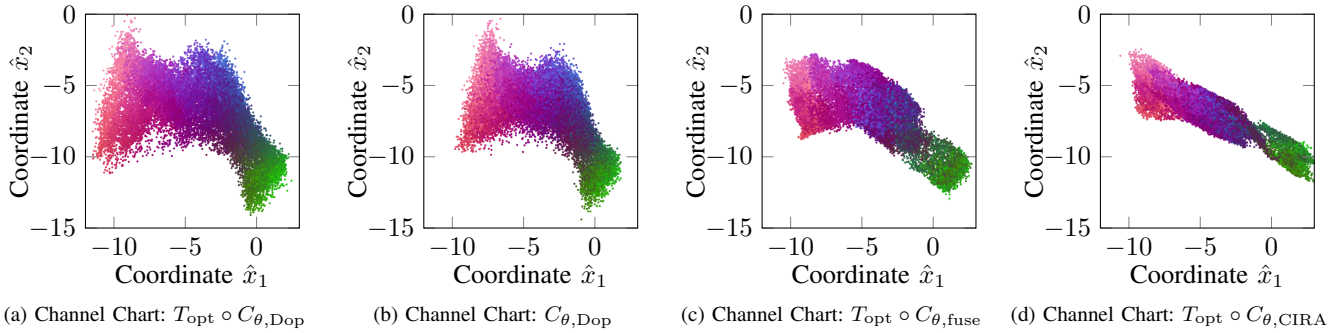


Fig. 4. Learned channel charts, FCF applied to S_{train} . Colors of points are preserved from color gradient applied in Fig. 1c.

D. Uncertainty

Estimating the uncertainty in the phase difference measurement $\Delta\varphi_{b_1,b_2}^{(l_1,l_2)}$, described by $\sigma_{b_1,b_2}^{(l_1,l_2)}$, plays an important role in the definition of a suitable loss function $\mathcal{L}^{(l_1,l_2)}$. For example, we must take into account that $\Delta\varphi_{b_1,b_2}^{(l_1,l_2)}$ is less precise if there is a long time delay $|t^{(l_2)} - t^{(l_1)}|$ between measurements (e.g., due to frequency drift, integration errors) and that the previously derived model for the relationship between displacement and phase only applies if the propagation channel is sufficiently line-of-sight (LoS)-like. Switching to continuous-time $t_1 = t^{(l_1)}$, $t_2 = t^{(l_2)}$ for notational reasons, we propose to compute $\sigma_{b_1,b_2}^{(l_1,l_2)}$ by using a heuristic that derives an instantaneous uncertainty $u_b(t) > 0$ from the delay spread of the channel between UE and BS antenna b . That is, $u_b(t)$ is large for high delay spreads (non-LoS) and small for low delay spreads (LoS). We then determine the standard deviation used for the loss function

$$\begin{aligned} \sigma_{b_1,b_2}^{(l_1,l_2)} &= \beta + \int_{t_1}^{t_2} (u_{b_1}(t) + u_{b_2}(t)) dt \\ &= \beta + (U_{b_1}(t_2) + U_{b_2}(t_2)) - (U_{b_1}(t_1) + U_{b_2}(t_1)) \end{aligned} \quad (6)$$

by integrating over these instantaneous uncertainties, where $U_b(t)$ denotes the antiderivative of $u_b(t)$ and β is a hyperparameter. In practice, channel measurements and hence uncertainty heuristics $u_b^{(l)}$ are only available at discrete times l , hence Eq. (6) turns into a summation and $U_b^{(l)}$ is found by numerical integration. By first computing $U_b^{(l)}$ for all $b \in \{1, \dots, B\}$, Eq. (6) can be solved for arbitrary combinations of b_1, b_2, l_1, l_2 with low computational complexity. The hyperparameter β is chosen to be some small value, and can be interpreted as the minimum uncertainty about $\Delta\varphi_{b_1,b_2}^{(l_1,l_2)}$ even for small time differences. It ensures that $\sigma_{b_1,b_2}^{(l_1,l_2)} > 0$ (no division by zero) and may be tweaked over training epochs. Future work may improve this uncertainty estimation step.

IV. FORWARD CHARTING FUNCTION TRAINING

We implement the FCF $\mathcal{C}_{\theta,\text{Dop}} : \mathbb{C}^{B \times N_{\text{sub}}} \rightarrow \mathbb{R}^2$, which maps CSI matrices $\mathbf{H}^{(l)}$ to positions $\hat{\mathbf{x}}^{(l)} = \mathcal{C}_{\theta,\text{Dop}}(\mathbf{H}^{(l)})$, as a NN. To use $\mathbf{H}^{(l)} \in \mathbb{C}^{B \times N_{\text{sub}}}$ in a NN that only operates on real numbers, an input layer extracts real part, imaginary part and logarithmic absolute values from a subset of time-domain channel taps $\mathcal{F}^{-1}\{\mathbf{H}^{(l)}\}$ (CIRs) for further processing. The

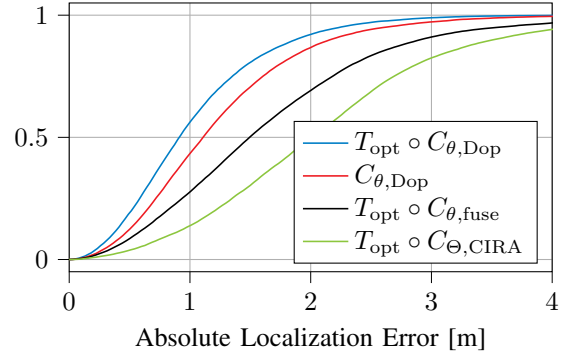


Fig. 5. Empirical CDFs of absolute localization errors (evaluated on S_{train})

NN is made up of 5 dense layers with rectified linear unit (ReLU) activation and 1024, 512, 256, 128 and 64 neurons each, followed by one output layer with linear activation and two neurons (two dimensions of position estimate $\hat{\mathbf{x}}$). We train the Siamese neural network in six epochs with increasing batch sizes and decreasing learning rates. In each epoch, the network is trained on 30 000 randomly selected pairs of datapoints.

Compared to previous work, e.g., [2], [3], there is nothing special about the NN architecture or training procedure. However, in contrast to previous work, we use the negated log-likelihood function from Eq. (4) as a loss function for self-supervised training of the NN in a Siamese NN configuration. Eq. (4) cannot be interpreted as a *dissimilarity metric* (compare [3]), i.e., as a spatial distance between datapoints (l_1, l_2) . This is because $\mathcal{L}^{(l_1,l_2)}$ not just depends on the distance between the two datapoints, but on the absolute coordinates $\hat{\mathbf{x}}^{(l_1)}$ and $\hat{\mathbf{x}}^{(l_2)}$. While this makes it harder to combine the Doppler effect-based Channel Charting approach with other approaches based on dissimilarity metrics, it enables the FCF to learn not just relative locations, but to locate datapoints in the global coordinate frame. Since Eq. (4) only operates on physically tangible quantities like distances and phase shifts, no rotation, scaling or translation (affine transformation) is required between channel chart and global coordinate frame.

V. EVALUATION

A. Baselines and Optimal Affine Transforms

Finding baselines in existing Channel Charting literature to benchmark the proposed method against is challenging, since other state-of-the-art Channel Charting techniques assume

TABLE I
PERFORMANCE COMPARISON: DOPPLER-BASED AND DISSIMILARITY METRIC-BASED CHANNEL CHARTING

	Dataset	MAE ↓	DRMS ↓	CEP ↓	R95 ↓	CT ↑	TW ↑	KS ↓	Figure
$T_{\text{opt}} \circ C_{\theta, \text{Dop}}$	$\mathcal{S}_{\text{train}}$	1.033 m	1.208 m	0.912 m	2.238 m	0.955	0.953	0.165	Fig. 4a
$C_{\theta, \text{Dop}}$	$\mathcal{S}_{\text{train}}$	1.235 m	1.431 m	1.108 m	2.607 m	0.953	0.951	0.170	Fig. 4b
$T_{\text{opt}} \circ C_{\theta, \text{fuse}}$	$\mathcal{S}_{\text{train}}$	1.653 m	1.923 m	1.495 m	3.541 m	0.913	0.893	0.264	Fig. 4c
$T_{\text{opt}} \circ C_{\theta, \text{CIRA}}$	$\mathcal{S}_{\text{train}}$	2.103 m	2.345 m	2.014 m	4.112 m	0.888	0.864	0.308	Fig. 4d
$C_{\theta, \text{Dop}}$	$\mathcal{S}_{\text{test}}$	1.346 m	1.540 m	1.227 m	2.757 m	0.933	0.929	0.200	—

MAE = Mean Absolute Error, DRMS = Distance Root Mean Square, CEP = Circular Error Probable, R95 = 95th percentile radius, CT = Continuity, TW = Trustworthiness, KS = Kruskal’s Stress, all metrics as defined in [3], [6]

time or phase synchronization and do not provide channel charts in the global coordinate frame. In the absence of a better alternative, we use dissimilarity metric-based Channel Charting with the CIR amplitude (CIRA) dissimilarity metric, proposed in [2], as a baseline. Lacking time synchronization, we time-shift the CIRs for each BS antenna individually such that the mean delay of the signal is zero. Furthermore, as proposed in [3], we introduce a baseline where we fuse the CIRA metric with a timestamp-based metric. In both cases, we use geodesic dissimilarities as in [2]. The trained NN-based FCFs are called $C_{\theta, \text{CIRA}}$ and $C_{\theta, \text{fused}}$, respectively. Since $C_{\theta, \text{CIRA}}$ and $C_{\theta, \text{fused}}$ produce channel charts whose coordinate frame may be arbitrarily transformed compared to the global coordinate frame, we find a linear mapping $T_{\text{opt}}(\mathbf{x}) = \hat{\mathbf{A}}\mathbf{x} + \hat{\mathbf{b}}$ that describes the optimal affine transformation from channel chart coordinates to global coordinates by solving

$$(\hat{\mathbf{A}}, \hat{\mathbf{b}}) = \arg \min_{(\mathbf{A}, \mathbf{b})} \sum_{l=1}^L \|\mathbf{A}\hat{\mathbf{x}}^{(l)} + \mathbf{b} - \mathbf{x}^{(l)}\|_2^2,$$

where $\hat{\mathbf{x}}^{(l)} = C_{\theta}(\mathbf{H}^{(l)})$ denotes the position estimate obtained through Channel Charting, and $\mathbf{x}^{(l)}$ is the “ground truth” position from the dataset. We write the composition of T_{opt} and C_{θ} , i.e., application of T_{opt} after the FCF, as $T_{\text{opt}} \circ C_{\theta}$. The performance for the baselines are computed *after* applying T_{opt} , which gives an unfair advantage to the baselines, but our approach outperforms the baselines regardless.

B. Results

Fig. 4 shows the learned channel charts, evaluated by applying the respective FCF on $\mathcal{S}_{\text{train}}$ and possibly also applying the respective optimal affine transform T_{opt} . Clearly, the proposed Doppler effect-based method manages to reconstruct the global geometry (L-shaped area) of the environment and even manages to locate datapoints in the global coordinate frame without subsequent transformation (Fig. 4b). As evidenced by Tab. I, $C_{\theta, \text{Dop}}$ not only produces visually more appealing channel charts, but also outperforms the baselines with respect to all considered performance metrics, even without applying T_{opt} (metrics highlighted in bold). We want to stress that evaluating on the training set (and not only on a separate test set) is meaningful, since Channel Charting is a self-supervised learning technique, but the last row in Tab. I indicates that performance on the test set is comparable anyway. Finally, we consider the empirical distribution of the localization error $\|\mathbf{x}^{(l)} - \hat{\mathbf{x}}^{(l)}\|_2$, as shown in the empirical cumulative distribution function (eCDF) diagram in Fig. 5. Unsurprisingly, $C_{\theta, \text{Dop}}$ also outperforms the baselines in the eCDF.

VI. OUTLOOK

Our results show that Channel Charting in global coordinates with only few BS antennas is possible by exploiting the Doppler effect, a feature of wireless CSI that has previously received little attention in the context of Channel Charting. While we only use Doppler effect-induced frequency shifts to derive a loss function, taking the Doppler effect into account for Channel Charting opens up several other exciting research directions. For example, one could derive a dissimilarity metric from frequency shifts, or use delay-Doppler domain features as FCF inputs. How to combine our Doppler effect-based loss function with dissimilarity-based or timestamp-based Channel Charting techniques remains an open question.

REFERENCES

- [1] C. Studer, S. Medjkouh, E. Gönültaş, T. Goldstein, and O. Tirkkonen, “Channel Charting: Locating Users within the Radio Environment using Channel State Information,” *CoRR*, vol. abs/1807.05247, 2018.
- [2] M. Stahlke, G. Yammine, T. Feigl, B. M. Eskofier, and C. Mutschler, “Indoor Localization with Robust Global Channel Charting: A Time-Distance-Based Approach,” *IEEE Transactions on Machine Learning in Communications and Networking*, 2023.
- [3] P. Stephan, F. Euchner, and S. ten Brink, “Angle-Delay Profile-Based and Timestamp-Aided Dissimilarity Metrics for Channel Charting,” *IEEE Transactions on Communications*, 2024.
- [4] J. Pihlajasalo, M. Koivisto, J. Talvitie, S. Ali-Löytty, and M. Valkama, “Absolute Positioning with Unsupervised Multipoint Channel Charting for 5G Networks,” in *2020 IEEE 92nd Vehicular Technology Conference (VTC2020-Fall)*. IEEE, 2020.
- [5] S. Taner, V. Palhares, and C. Studer, “Channel Charting in Real-World Coordinates,” in *2023 IEEE Global Communications Conference*, 2023.
- [6] F. Euchner, P. Stephan, and S. t. Brink, “Augmenting Channel Charting with Classical Wireless Source Localization Techniques,” in *57th Asilomar Conference*, 2023.
- [7] Y.-T. Chan and F. L. Jardine, “Target localization and tracking from Doppler-shift measurements,” *IEEE Journal of Oceanic Engineering*, vol. 15, no. 3, pp. 251–257, 1990.
- [8] I. Shames, A. N. Bishop, M. Smith, and B. D. O. Anderson, “Doppler Shift Target Localization,” *IEEE Transactions on Aerospace and Electronic Systems*, vol. 49, no. 1, pp. 266–276, 2013.
- [9] M. Stahlke, G. Yammine, T. Feigl, B. M. Eskofier, and C. Mutschler, “Velocity-Based Channel Charting with Spatial Distribution Map Matching,” *arXiv preprint arXiv:2311.08016*, 2023.
- [10] S. Taner, M. Guillaud, O. Tirkkonen, and C. Studer, “Channel Charting for Streaming CSI Data,” in *2023 57th Asilomar Conference*, 2023.
- [11] F. Euchner, M. Gauger, S. Dörner, and S. ten Brink, “A Distributed Massive MIMO Channel Sounder for “Big CSI Data”-driven Machine Learning,” in *25th ITG Workshop on Smart Antennas*, 2021.
- [12] F. Euchner, P. Stephan, M. Gauger, and S. ten Brink, “Geometry-Based Phase and Time Synchronization for Multi-Antenna Channel Measurements,” in *2022 IEEE Globecom Workshops*. IEEE, 2022.
- [13] D. R. Brown, G. B. Prince, and J. A. McNeill, “A method for carrier frequency and phase synchronization of two autonomous cooperative transmitters,” in *IEEE 6th Workshop on Signal Processing Advances in Wireless Communications*, 2005. IEEE, 2005, pp. 260–264.
- [14] L. Zhao, Y. Yang, Q. Xiong, H. Wang, B. Yu, F. Sun, and C. Sun, “A Signature Based Approach Towards Global Channel Charting with Ultra Low Complexity,” *arXiv preprint arXiv:2403.20091*, 2024.